Tropical-cyclone convection: the effects of a near tropical storm strength vortex on deep convection

Gerard Kilroy[a*] and Roger K. Smith[a]

[a] *Meteorological Institute, Ludwig-Maximilians University of Munich, Munich, Germany*

*Correspondence to: Gerard Kilroy, Meteorological Institute, Ludwig-Maximilians University of Munich, Theresienstr. 37, 80333 Munich, Germany, Email: gerard.kilroy@lmu.de

Idealized numerical model simulations are used to investigate the generation and evolution of vertical vorticity by deep convection in a warm-cored vortex of near tropical storm strength. Deep convective updraughts are initiated by thermal perturbations located at different radii from the vortex axis. It is found that, as the location of the thermal perturbation is moved away from the axis of rotation, the updraught that results becomes stronger, the cyclonic vorticity anomaly generated by the updraught becomes weaker, the structure of the vorticity anomaly changes and the depth of the anomaly increases. For an updraught along or near the vortex axis, the vorticity anomaly has the structure of a monopole and little or no anticyclonic vorticity is generated in the core. Vorticity dipoles are generated in updraughts near or beyond the radius of maximum tangential wind speed and this structure reverses in sign with height. In all cases the anomalies persist long after the initial updraught has decayed. Implications of the results for understanding the vorticity consolidation during tropical cyclogenesis are discussed.

The effects of eddy momentum fluxes associated with a single updraught on the tangential-mean velocity tendency are investigated and a conceptual framework for the interpretation of these eddy fluxes is given. The simulations are used to appraise long standing ideas suggesting that latent heat release in deep convection occurring in the high inertial stability region of a vortex core is "more efficient" than deep convection outside the core in producing temperature rise in the updraught.

Key Words: tropical cyclones, rotating deep convection, vortical hot towers

Received March 10, 2016; Revised ; Accepted

Citation: ...

1. Introduction

The pioneering numerical studies of tropical cyclogenesis by Hendricks *et al.* (2004) and Montgomery *et al.* (2006) highlighted the potentially important role of vorticity amplification by rotating deep convection in the dynamics of genesis. In these and subsequent studies (Tory *et al.* 2006a,b, 2007, Nolan 2007, Nguyen *et al.* 2008, Shin and Smith 2008, Fang and Zhang 2010, Ngyuen *et al.* 2011, Gopalakrishnan et al. 2011, Bao *et al.* 2012, Persing *et al.* 2013, Nicholls and Montgomery 2013, Davis 2015), the progressive aggregation, merger and axisymmetrization of the convectively-enhanced vorticity anomalies aided by the convectively-induced system-scale convergence are found to be prominent features in both the formation and intensification of tropical cyclones in models. Recent reviews of these studies are given by Montgomery and Smith (2014) and Smith and Montgomery (2015).

Motivated by the early findings and in parallel with subsequent work, there has been a series of numerical investigations of vorticity production by *individual* deep convective clouds in rotating environments with background flows of increasing complexity (Rozoff 2007, Wissmeier and Smith 2011, Kilroy and Smith, 2012, 2015 (henceforth KS15), Kilroy *et al.* 2014 (henceforth KSW14)). Such studies are pertinent to developing an understanding of the evolution of more complex vortex systems involving local vorticity amplification by multiple deep clouds. A review of the earlier studies by Rozoff (2007), Wissmeier and Smith (2011) and Kilroy and Smith (2012), which considered quiescent environments, and those which included uniform horizontal and/or vertical shear is given by KSW14.

KSW14 investigated the effects of a *unidirectional* boundary-layer wind structure on storm structure, especially on vertical vorticity production. They investigated also the combined effects of horizontal and vertical shear on vertical vorticity production, with and without background rotation. They noted that in tropical depressions and tropical cyclones, the tangential wind speed decreases with height above a shallow boundary layer so that the sign of the radial vorticity component changes sign at some low level, typically on the order of a few kilometres. It was shown that the tilting of horizontal vorticity by a convective updraught in this environment leads not only to dipole patterns of vertical vorticity, but also to a reversal in sign of the vorticity with height. The results are in contrast to the classical mid-latitude thunderstorm case, where the wind increases in strength with height so that the local cross-wise vorticity has a single sign (see Ramsay and Doswell 2005; their Fig. 1). These findings add a layer of complexity to interpretations of the aggregation of convectively induced cyclonic vorticity anomalies in terms of barotropic dynamics (e.g. Nguyen et al., 2008).

Another complication in the context of tropical cyclones is that there is a significant radial wind component in the boundary layer, an effect that was omitted in KSW14. KS15 carried out a further series of numerical experiments to investigate the effects of a vortex boundary-layer wind profile on the generation of vertical vorticity in tropical deep convection. In these experiments the wind hodograph turned clockwise with height within the boundary layer. Situations were considered in which there was either no vertical shear above the boundary layer, or negative vertical shear appropriate to a warm-cored vortex. Deep convection growing in these environments develops dipole structures of vertical-vorticity in which the cyclonic gyre is favoured and persists longer than the anticyclonic one. The orientation of the dipole at a particular height is determined partly by that of the ambient horizontal vortex lines, which rotate with height, and also by the vertical advection of vertical vorticity from below. When negative vertical shear above the boundary layer is considered the vorticity dipole reverses in sign at some height, but because of the strong vertical advection of the dipole from below, the reversal in sign occurs at a much higher altitude than would be explained by the linear theory of Rotunno and Klemp (1982).

In the present paper we go one step further in realism and investigate vertical vorticity generation in an initially-balanced, warm-cored vortex. In such a vortex there are spatial variations of temperature, vorticity and tangential wind, all of which could influence the development of vertical vorticity within deep clouds growing in such an environment. Vertical vorticity developing within the radius of maximum tangential winds (where the flow regime is vorticity dominated) is expected to be longer lived, whereas that developing outside the radius of maximum winds (where the flow is strain dominated) is expected to be weaker and more filamented (Rozoff *et al.* 2009). Clouds developing outside the radius of maximum winds are more susceptible also to the entrainment of ambient air (Rozoff *et al.* 2006), which will affect the maximum updraught strength. The aim of this study is to highlight and quantify such effects.

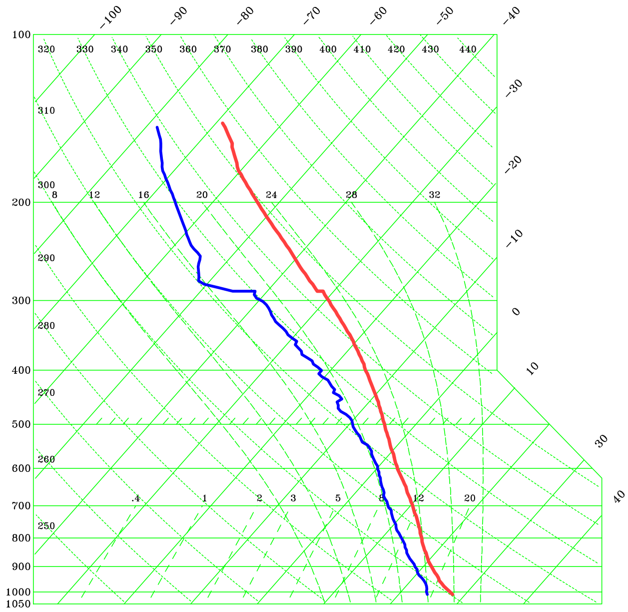

Figure 1. Skew-T log-p diagram showing the temperature (right solid curve) and dew point temperature (left solid curve) of the Karl pouch sounding used in this study.

The plan is to initiate deep convection with a thermal perturbation at different radial locations in a warm-cored vortex and examine the generation and decay of vertical vorticity during the lifetime of the cloud. Several locations are chosen, both inside and outside the radius of maximum tangential winds. We examine also the contributions of deep convective clouds on the evolution of the vortex itself by analysing azimuthally-averaged eddy terms in the tangential momentum equation (Persing *et al.* 2013). These calculations are seen as the next step to understanding how deep convective clouds generate vertical vorticity at different radial locations within tropical cyclones.

The paper is organized as follows. A brief description of the numerical model is given in section 2 and the configuration of the experiments is described in section 3. The results are presented in sections 4 and a discussion of the relevance of these results for tropical cyclone genesis and intensification is given in section 5. The contributions of deep convective clouds on the evolution of the vortex are discussed in section 6, and a discussion of the "efficiency" of deep convection in relation to its location in the vortex is given in section 7. The conclusions are given in section 8.

2. The numerical model

The numerical simulations relate to the prototype problem for tropical cyclone intensification, which considers the evolution of a prescribed, initially cloud-free axisymmetric weak vortex in a quiescent environment on an f-plane as articulated in Nguyen *et al.* (2008). They are carried out using the numerical model CM1 version 16, a non-hydrostatic and fully compressible cloud model (Bryan

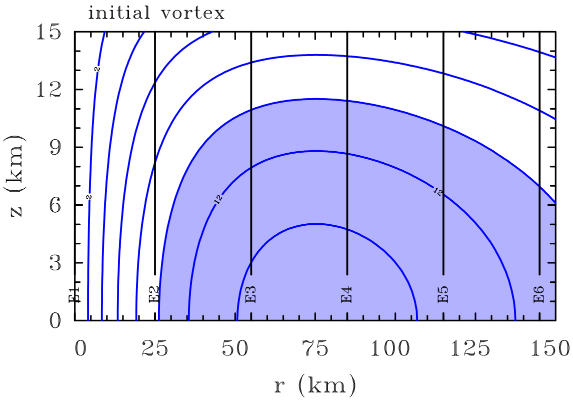

Figure 2. Vertical cross section of the initial vortex structure and the locations of the initial thermals. Contours: V wind component contoured every 2 m s^{-1}, with blue shading for regions stronger than 10 m s^{-1}. The locations of the initial thermal perturbation for the various experiments are indicated by vertical lines labelled E1, E2, etc.

and Fritsch 2002)* in the three-dimensional configuration described by Persing *et al.* (2013) and Črnivec *et al.* (2016), except that a larger inner grid-mesh region with constant grid spacing is used here. Specifically, the outer domain is 1500 × 1500 km in size with variable spacing increasing to 10 km near the domain boundaries. The inner domain is 300 × 300 km in size and has a grid spacing of 500 m. The domain has 40 vertical levels extending to a height of 25 km. The vertical grid spacing expands gradually from 50 m near the surface to 1200 m at the top of the domain.

In brief, the model has prediction equations for the three components of the velocity vector, specific humidity, suspended liquid, perturbation Exner function, and perturbation density potential temperature, where perturbation quantities are defined relative to a prescribed hydrostatic basic state. A simple warm-rain scheme is used in which rain has a fixed fall speed of 7 m s^{-1}. For simplicity, ice microphysical processes and dissipative heating are not included in these experiments. The large time step is 5 seconds and the integration time is 2 h. There are ten small time steps for each large time step to resolve fast-moving sound waves. A Rayleigh damping layer is added at heights above 20 km to suppress the artificial reflection of internal gravity waves from the upper boundary. The e-folding time scale for this damping is 5 min. Rayleigh damping is applied also within 100 km of the lateral boundaries, which are rigid walls. Radiative effects are represented by adopting a simple Newtonian cooling approximation with a time scale of 12 h. Following Rotunno and Emanuel (1987), the magnitude of the cooling rate is capped at 2 K per day.

2.1. *Thermodynamic sounding*

All experiments use the reference sounding shown in Fig. 1. It is constructed from a day mean of dropsonde soundings in the pouch region of pre-genesis tropical storm Karl on 12 Sep 2010, obtained during the Pre-Depression Investigation of Cloud Systems in the Tropics (PREDICT) field campaign (see Montgomery *et al.* 2012 for more details). This sounding has a CAPE† of 1950 J kg^{-1}, a Convection Inhibition (CIN)‡ of 47 J kg^{-1} and a Total Precipitable Water (TPW) value of 61 kg m^{-2}. The surface temperature is 302.15 K.

2.2. *Initial vortex and wind profiles*

As in Črnivec *et al.* (2016) and Kilroy *et al.* (2016a), the prescribed initial vortex is axisymmetric and in thermal wind balance. The initial tangential wind speed has a maximum of 15 m s^{-1} at the surface at a radius of 75 km from the centre of circulation. The tangential wind component decreases sinusoidally with height, becoming zero at a height of 20 km. Above this height, the tangential wind is set to zero. The balanced pressure, density and temperature fields consistent with this prescribed tangential wind distribution are obtained using the method described by Smith (2006). A vertical cross section of the initial vortex is shown in Fig. 2, along with the locations of the initial thermal perturbations used for all experiments.

2.3. *Representation of vertical vorticity*

The calculations are carried out on an f-plane with the Coriolis parameter $f = 2.53 \times 10^{-5}$ s^{-1}, corresponding to a latitude of 10°N. The background vertical vorticity associated with the initial vortex is represented in Fig. 3.

2.4. *Initiation of convection*

Convection is initiated by a symmetric thermal perturbation with a horizontal radius of 10 km and a vertical extent of 1 km. The temperature excess has a maximum at the surface at the centre of the perturbation and decreases monotonically to zero at the perturbation's edge. The perturbation centre coincides with the centre of the domain. In general, the details of the ensuing convection such as the updraught depth and the maximum updraught strength will depend on the amplitude and spatial structure of the thermal perturbation. A maximum temperature perturbation of 3.5 K is used in all experiments, which is 0.5 K larger than that used in KW14, but the same as that used in Wissmeier and Smith (2011). The water vapour mixing ratio in the warm bubble is increased so that the relative humidity is essentially the same as the surrounding environment, and this moisture adjustment does not lead to noticeable differences in TPW between the experiments.

3. The numerical experiments

We describe eight numerical experiments, details of which are summarized in Fig. 3. Shown are the distance of the

*For a complete description of the three-dimensional model and variable definitions see the technical document "The governing equations for CM1", available for download at http://www.mmm.ucar.edu/people/bryan/cm1 and available also from G. Bryan at the National Center for Atmospheric Research. For a complete description of the axisymmetric version of CM1, see the paper by Bryan and Rotunno (2009).

†We remind the reader that CAPE is a parcel quantity that typically has a strong negative vertical gradient in the lower troposphere. For this reason, the values cited herein are based on an average for air parcels lifted from the surface and at 100 m intervals above the surface to a height of 500 m. Since the calculation of CAPE is a non-linear function of temperature and moisture, we prefer this method to one based on averaged values of temperature and mixing ratio through a surface-based layer of air with some arbitrarily-prescribed depth.

‡Like CAPE, CIN is a quantity that refers also to an air parcel. Rather than computing an average up to 500 m as for CAPE, it seems physically more reasonable to examine the minimum value of CIN up to this level.

Expt.	w_{max}	w_{min}	w_{1max} m s^{-1}	$t(w_{1max})$ min	w_{4max} m s^{-1}	$t(w_{4max})$ min	w_{6max} m s^{-1}	$t(w_{6max})$ min	w_{1min} m s^{-1}	$t(w_{1min})$ min
1	8.6	-2.9	4.2	20	8.6	34	2.3	40	-0.85	42
2	13.2	-3.4	5.2	20	12.2	32	11.8	36	-1.0	42
3	14.8	-3.9	5.6	22	13.3	30	14.3	34	-1.2	42
4	15.5	-4.3	5.8	22	14.2	30	15.5	34	-1.2	38
5	16.3	-4.4	6.0	22	14.7	30	16.0	34	-1.2	38
6	16.9	-4.5	6.2	22	15.1	30	16.1	34	-1.3	38
7	12.6	-3.4	4.9	20	11.6	32	10.8	36	-1.1	42
8	16.3	-4.3	6.1	20	14.3	28	15.7	32	-1.4	40

Table I. Maximum vertical velocity, wN_{max}, and minimum vertical velocity, wN_{min}, at a height of N km and the times at which they occur, $t(wN_{max})$ and $t(wN_{min})$, respectively in Expts. 1-8. The first two columns display the maximum and minimum velocities throughout the domain and the two hour integration time.

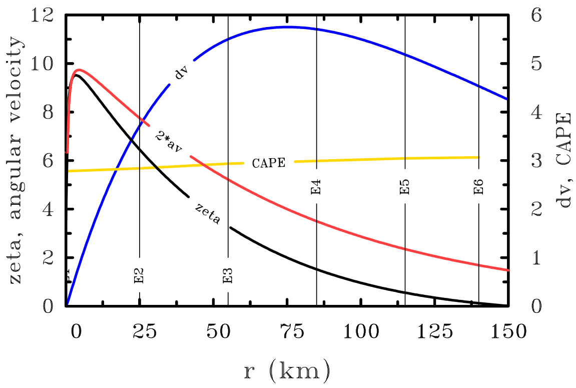

Figure 3. Radial variation of relative vorticity (zeta) and twice the relative angular velocity (2*av) at the surface, vertical shear (dv), and CAPE for the initial vortex shown in Figure 2. The locations of the initial thermal perturbation for the various experiments are indicated by vertical lines labelled E1, E2, etc.

initial thermal perturbation from the circulation centre and some environmental measures at this location, including the bulk shear, twice the angular velocity, the relative vorticity, and the Convective Available Potential Energy (CAPE). Further details of the experiments and their purpose are given in the appropriate sections.

The warm bubble in Expt. 1 is located at the vortex centre, which has high values of relative vorticity (see Fig. 3). Here, there is no vertical shear over the entire troposphere, but the CAPE[§] is lower than that in other experiments due to the increased temperature associated with the warm cored balanced vortex. In general, the CAPE increases the further the warm bubble is located from the vortex axis, while the relative vorticity decreases in strength. The shear magnitude increases out to a radius of 75 km (the radius of maximum winds). Outside this radius, the shear magnitude decreases in strength. Three experiments have the initial thermal located inside the radius of maximum winds and three outside of that. The locations of the initial thermals for all experiments are shown in Figs. 2 and 3.

Experiments 7 and 8 are repeats of Expts. 2 and 4 respectively, but with surface friction switched off. These experiments are performed to provide a less cluttered depiction of the azimuthally averaged eddy terms discussed in section 6.

[§]The calculation of CAPE in Fig. 3 includes the initial moist thermal perturbation.

As a broad means for making quantitative comparisons of the various experiments, Table I gives details of the maximum updraught and downdraught strengths at selected heights for all experiments and Table II lists the corresponding maximum and minimum vertical vorticity in these experiments.

4. Results

The principal features of updraught evolution in Expts. 1-6 are as follows.

4.1. Vertical velocity

Figure 4 shows time-height cross sections of maximum[¶] vertical velocity in all experiments and Table I gives details of the maxima and minima at selected heights.

In Expt. 1 the maximum updraught and downdraught strengths, w_{max} and w_{min}, are 8.6 m s^{-1} and 2.9 m s^{-1}, respectively (Table I). The maximum occurs at a height of 4 km at 34 min. The maximum vertical velocity at a height of 6 km is only 2.3 m s^{-1}, suggesting that the cloud does not penetrate much further above this height. The maximum vertical velocity increases monotonically in strength at all heights and times the further the initial thermal is located from the vortex axis. In Expt. 6, w_{max} and w_{min} are 16.9 m s^{-1} and 4.5 m s^{-1}, respectively. The maximum vertical velocity at a height of 6 km in this experiment is 16.1 m s^{-1}, much larger than that in Expt. 1.

Not only is w_{max} larger in convection developing further away from the vortex axis, the height at which this maximum occurs increases also (Fig. 4). For example, the convective cell in Expt. 1 (panel a) barely extends to a height of 6 km, but that in Expt. 6 (panel f) extends to a height of just over 10 km. There appears also to be secondary convection occurring in some experiments, most notably when the initial thermal is located further from the vortex axis. These secondary cells are a result of the stronger downdraughts and larger negative buoyancy at low levels (not shown) associated with the outer core convection. The lower CIN at radii outside the vortex core

[¶]The evolution of the updraught associated with the rising thermal bubble is similar to that described in KS15. The presence here of an ambient shear means that updraughts and downdraughts are tilted so that the extrema of vertical velocity and vertical vorticity occur at different spatial locations at different times. This feature which makes a single cross-section for updraughts and downdraught extrema or for positive and negative vorticity inappropriate.

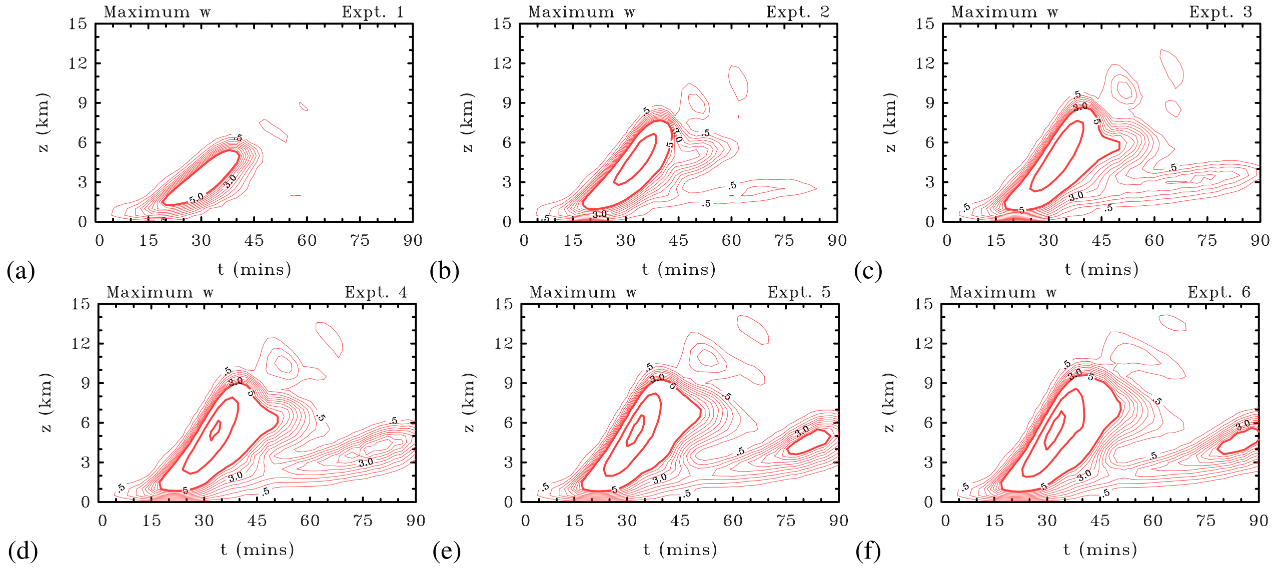

Figure 4. Time-height series of maximum vertical velocity in Expts. 1-6. Contour intervals: vertical velocity, thin contours 0.5 m s^{-1}, thick contours 5 m s^{-1}.

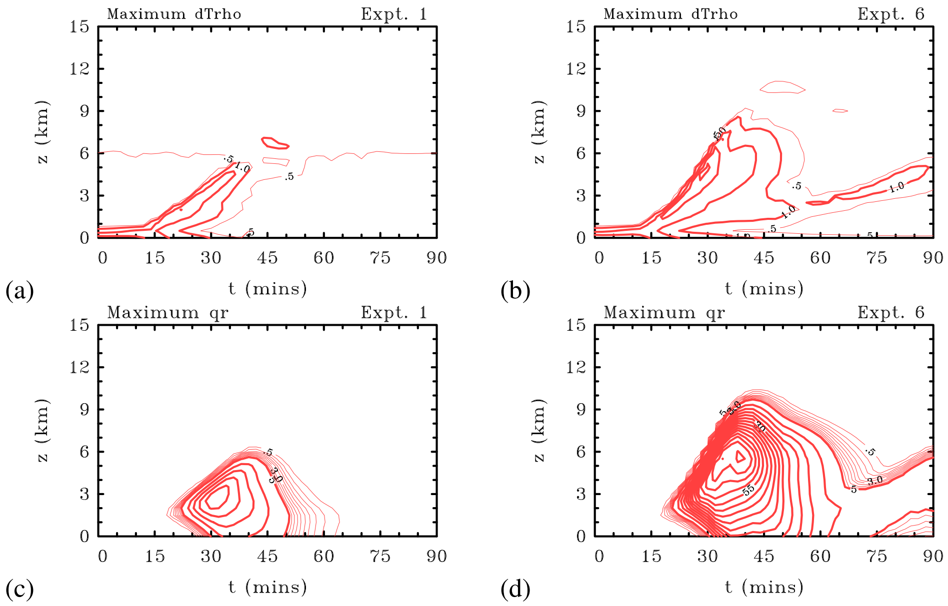

Figure 5. Time-height series of (a,b) maximum density temperature difference and (c,d) maximum cloud rain in Expts. 1 and 6. Contour intervals: dTrho, thin contour 0.5 K, thick contours 1.0 K. Cloud rain,thin contours 0.5 g kg^{-1}, thick contours 5 g kg^{-1}

(not shown) makes it easier for the spreading cold pools to lift environmental air to its level of free convection.

4.2. Buoyancy and cloud rain

Figure 5 shows time-height cross sections of maximum density temperature difference (top panels, a measure of the cloud buoyancy including the effects of water loading) and the maximum rain water (bottom panels) for Expts. 1 and 6. The far field sounding is used as the reference temperature to calculate buoyancy. The buoyancy produced by latent heat release is much weaker in Expt. 1 than in Expt. 6 and the height at which the maximum buoyancy occurs is much lower in Expt. 1. The amount of rainfall produced is much lower in Expt. 1, a result expected with weaker convection. In panel (a), the system buoyancy associated with the warm cored vortex is clearly noticeable.

4.3. Vertical vorticity

4.3.1. Vertical vorticity extrema

Details of the maximum and minimum vertical vorticity at selected heights for all experiments are included in Table II. In Expt. 1, the overall maximum $\zeta_{max} = 11.6 \times 10^{-2}$ s^{-1} and occurs at the surface. In the experiments where convection is located at increasing distances from the vortex axis, ζ_{max} decreases monotonically with the smallest maximum value occurring in Expt. 6 (4.2 $\times 10^{-2}$ s^{-1}). In Expts. 2-6 the maximum occurs at a height of 500 m. The maximum cyclonic vorticity occurs at relatively low

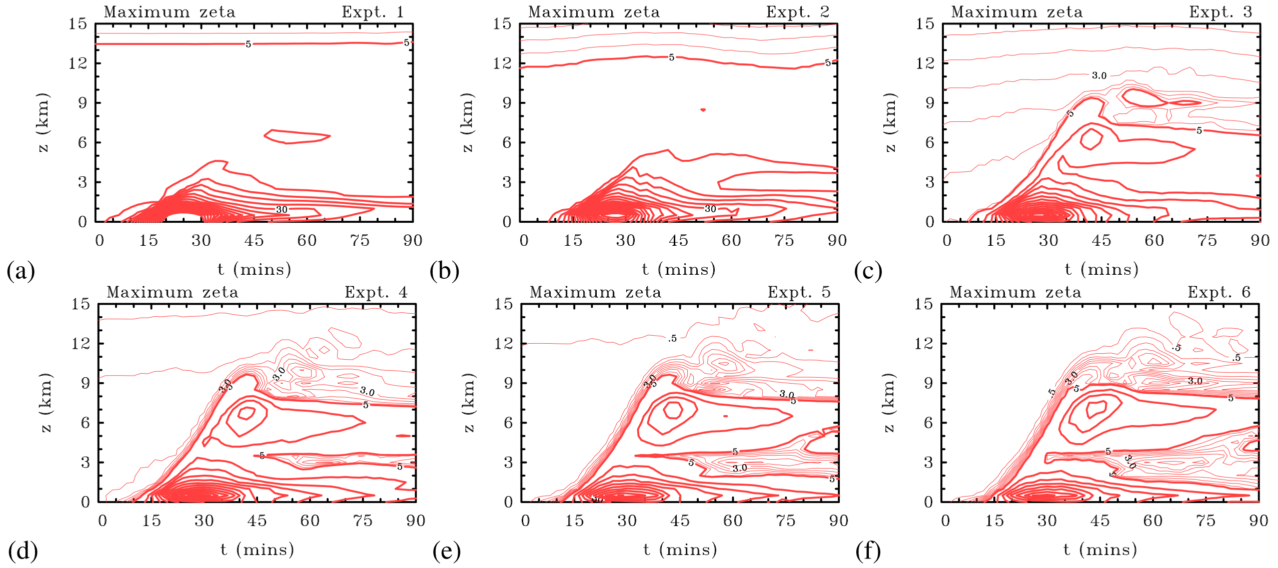

Figure 6. Time-height series of maximum vertical vorticity in Expts. 1-6. Contour intervals: vertical vorticity, thin contours 0.5×10^{-3} s^{-1} to 4.5×10^{-3} s^{-1}, thick contours 5×10^{-3} s^{-1}.

Expt.	ζ_{max} 10^{-3} s^{-1}	$z(\zeta_{max})$ km	$\zeta_{0.5max}$ 10^{-3} s^{-1}	$t(\zeta_{0.5max})$ min	ζ_{1max} 10^{-3} s^{-1}	$t(\zeta_{1max})$ min	ζ_{4max} 10^{-3} s^{-1}	$t(\zeta_{4max})$ min	ζ_{1min} 10^{-3} s^{-1}	$t(\zeta_{1min})$ min	ζ_{4min} 10^{-3} s^{-1}	$t(\zeta_{4min})$ min
1	115.7	0.0	102.3	24	71.8	24	10.2	54	-5.8	22	0	-
2	96.9	0.5	96.9	28	74.6	26	17.0	32	-9.6	24	-3.5	30
3	75.5	0.5	75.5	30	55.4	28	11.3	30	-16.4	28	-11.4	30
4	63.3	0.5	63.3	28	44.5	30	9.9	28	-20.8	28	-13.6	30
5	50.8	0.5	50.8	28	36.1	30	8.3	28	-22.5	30	-13.2	28
6	41.5	0.5	41.5	30	29.6	34	7.3	36	-21.7	30	-12.1	28
7	119.1	0.0	98.0	26	73.4	26	15.0	32	-7.6	22	-2.2	32
8	56.0	0.0	45.2	30	35.0	30	13.7	38	-7.2	22	-11.4	30

Table II. Maximum of the vertical component of relative vorticity, ζN_{max}, at heights N of 500 m, 1 km and 4 km and the times at which they occur, $t(\zeta N_{max})$, in Expts. 1-8. Shown also is minimum of this vorticity component at a height of 1 km and 4 km, together with the time at which they occur.

altitudes compared to the those in the KSW14 experiments on account of both the absence of strong background horizontal vorticity at upper levels and because of the large background relative vorticity at low levels associated with the vortex. KSW14 and KW14 showed that vertical vorticity produced at low levels was mainly the result of the stretching of existing vertical vorticity, whereas vertical vorticity produced above the boundary layer was mostly due to the tilting of horizontal vorticity. Both of these studies showed also that the vorticity dipole produced by tilting reversed in sign at some height when the background horizontal vorticity changes sign at the top of the boundary layer. An unexpected result was the large contribution by the vertical advection term, which resulted in vorticity dipoles that did not reverse in sign at the heights they were expected to (i.e. the vorticity dipole at given height above the boundary layer did not match the orientation expected by the horizontal vorticity at that height, rather by the horizontal vorticity at lower levels).

The monotonic decrease in ζ_{max} with increasing distance from vortex core occurs at mostly all heights, except in Expt. 1 above 1 km. This reasons for this is that the strength of the updraught is weaker in this experiment at upper levels and there is no background horizontal vorticity at this location so that tilting does not play a role in generating vorticity at upper levels.

The minimum vorticity at a height of 1 km, ζ_{1min}, is -0.6×10^{-2} s^{-1} in Expt. 1, and becomes progressively larger in magnitude as the convection is located further from the vortex axis, except in Expt. 6 which is furthest from the axis. Beyond the radius of maximum tangential wind speed, the toroidal vorticity begins to decrease in magnitude with radius whereupon, even though there is an increase in the vertical velocity, the contribution to vorticity production by tilting decreases beyond some radius. In all experiments ζ_{1max} is stronger in magnitude than ζ_{1min}, although the difference is much larger when the convection occurs closer to the vortex axis. Note that at a height of 4 km this result is not always true, with the minimum stronger in magnitude in the calculations where convection occurs outside the radius of maximum winds.

In the experiments where convection occurs outside the radius of maximum winds, there are stronger magnitudes of maximum and minimum vertical vorticity at a height of 6 km than at 4 km (not shown). For example, in Expt. 5 ζ_{6max} is 1.9×10^{-2} s^{-1}, while ζ_{6min} is -1.9×10^{-2} s^{-1}. There are similar values for Expts. 4 and 6. These identical values of maximum and minimum vertical vorticity are tell-tale signs that vorticity production occurs primarily by tilting at this height.

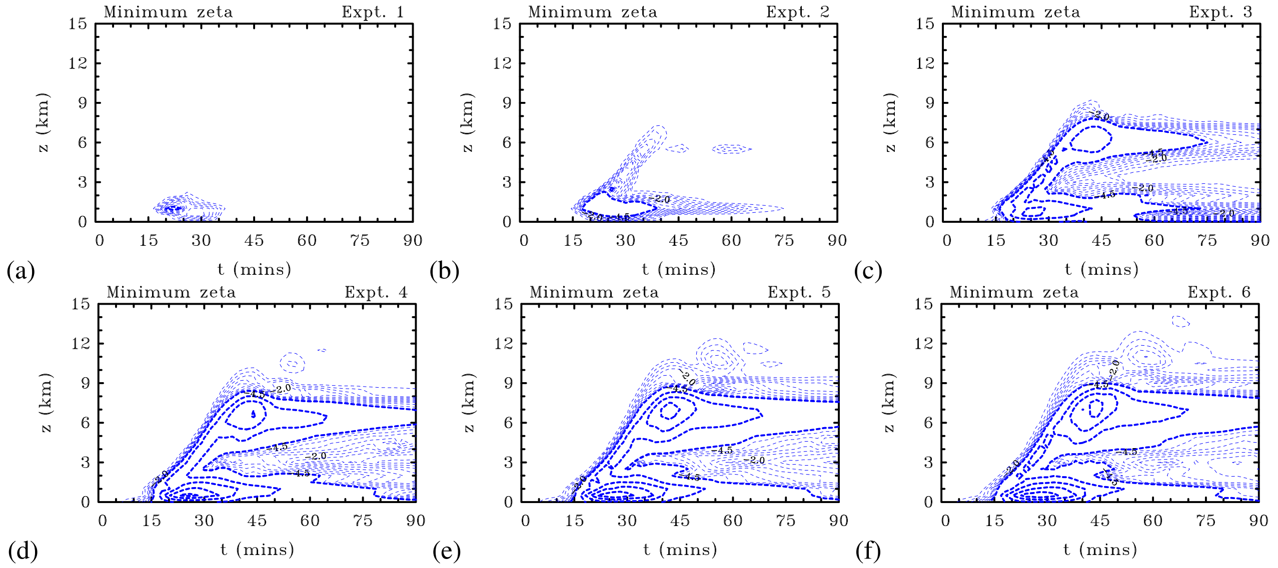

Figure 7. Time-height series of minimum vertical vorticity in Expts. 1-6. Contour intervals: vertical vorticity, thin contours 0.5×10^{-3} s^{-1} to 4.5×10^{-3} s^{-1}, thick contours 5×10^{-3} s^{-1}.

4.3.2. Vorticity maximum evolution

Figures 6 and 7 show time-height cross sections of the maximum and minimum vertical vorticity in all experiments (these extrema may not occur at the same horizontal location). Note that significant vertical vorticity is generated up to a height of about 5 km in Expt. 1 and up to a height of 9 km in Expt. 6 (compare panels a and f).

The maximum cyclonic vorticity occurs between the surface and a height of 1 km and persists longest within this height range. In the experiments located near the radius of maximum winds there is significant vertical vorticity generated between heights of 5 and 9 km due to tilting of background horizontal vorticity.

In Expts. 1 and 2 there is only minor development of anticyclonic vorticity, mostly below a height of 3 km, while in Expts. 3-6, significant anticyclonic vorticity is generated both near the surface and between heights of 5 to 9 km.

Figure 8 shows the evolution of the maximum and minimum vertical vorticity in all experiments. As we have seen in Table II the vorticity maximum decreases monotonically with convection located further from the vortex axis. An important result is that an enhanced ζ_{max} persists until the end of the simulation in all experiments. In Expt. 1 the final ζ_{max} is about three times larger than the initial ζ_{max}. The inner core experiments (Expts. 1 and 2) develop a relatively weak vorticity minimum and this does not persist until the end of the simulation. In Expts. 3-6 the minimum persists beyond the life time of the cloud, until the end of the simulation.

4.3.3. Horizontal structure of vorticity

Figure 9 shows horizontal cross sections of the vertical component of relative vorticity in Expt. 1 at heights of 500 m and 2 km at 20, 30 and 40 min. Shown also in the bottom panels are similar horizontal cross sections at a height of 2 km for Expt. 2. Regions of ascent exceeding 1 m s^{-1} and subsidence with magnitude exceeding 1 m s^{-1} are shown in black contours. Values of density temperature difference (dTrho) above 1 K are shown also. At a height of 500 m in Expt. 1 there is a strong vertical vorticity monopole at all times. At 20 min this monopole is encircled by positive vertical motion which is replaced by a small scale downdraught at 40 min. At 30 min there is an annulus of weak anticyclonic vertical vorticity associated with a reduction in relative vorticity due to outflow at this level as the thermal pushes through it. However, this negative anomaly does not persist and is not present at this height at 40 min. At a height of 2 km a buoyant updraught is present at 20 and 30 min, but a core of strong (greater than 20×10^{-3} s^{-1}) vertical vorticity develops only after 20 min. By 40 min there remains a core of enhanced vorticity. Despite the initial thermal being located in a region of background vertical shear in Expt. 2 (see Fig. 3) there exists also a strong monopole of vertical vorticity at a height of 2 km, and vertical motion (stronger than 1 m s^{-1}) occurs at this height at 40 min.

Figure 10 shows similar plots as in Fig. 9 for Expt. 4 at heights of 500 m, 2 km and 6 km. At 20 min at a height of 500 m there is a vorticity tripole. The weaker anticyclonic anomaly to the right of the updraught is associated with toroidal vorticity. To understand this structure, we note that the buoyancy of the rising thermal creates toroidal vorticity, which, together with ambient horizontal and vertical vorticity is tilted by the horizontal gradient of vertical velocity and stretched by the vertical gradient thereof. This feature was noted also in KSW14. The prominent vertical vorticity feature at this height is the dipole which is co-located with the updraught and positive buoyancy. At 30 min the updraught is still present, although by 40 min there is only a small region of downdraught. The tripole feature is evident at a height of 2 km at 30 and 40 min, while there is positive buoyancy and upward motion at all three times shown at this height. At a height of 6 km the updraught is just breaking through at 30 min, while at 40 min there is positive vertical motion. The dipole at this height at 40 min has reversed in sign when compared to that at lower levels, a result found also in KS15 and KSW14.

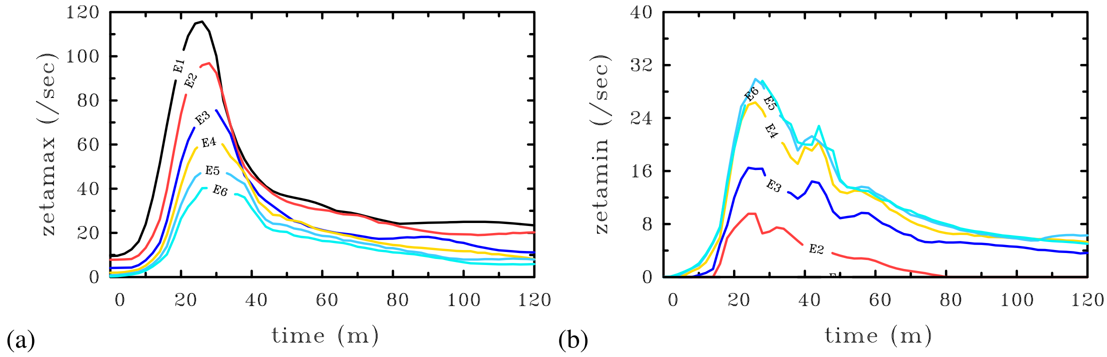

Figure 8. Time height plots of (a) maximum and (b) minimum vertical vorticity in all experiments.

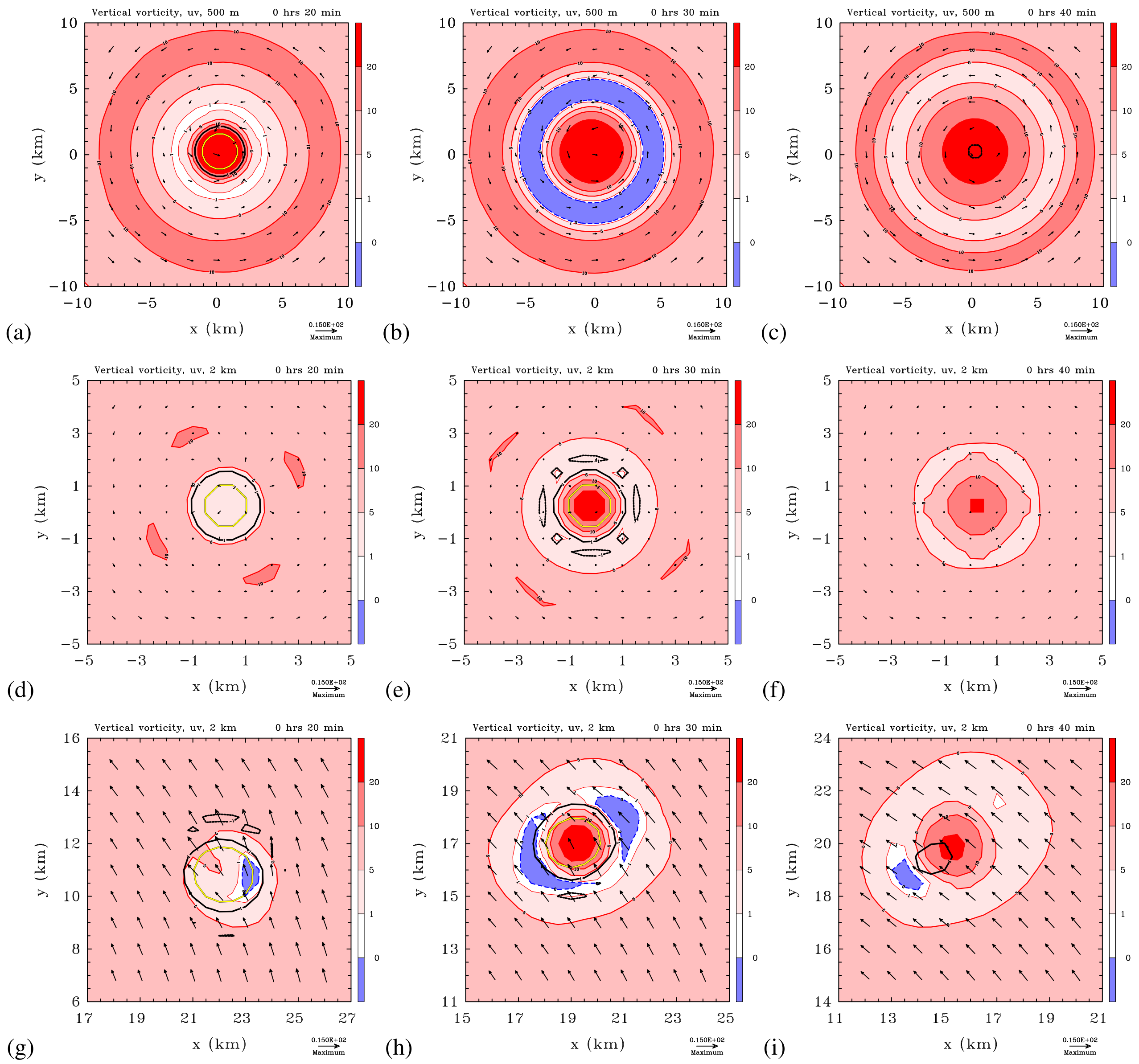

Figure 9. Horizontal cross sections of the vertical vorticity (shaded), vertical velocity (black contours), density temperature difference (yellow contours) and wind vectors at heights of 500 m (top panels) and 2 km (middle panels) at 20, 30 and 40 min for Expt. 1. The bottom panels show the same plots as the middle panels but for Expt. 2. Vorticity shading given in the label bar, while the wind vectors should be compared to the reference vector on the bottom right of each panel. Contour intervals: vertical vorticity thin contour 1×10^{-3} s^{-1}, thick contour 5×10^{-3} s^{-1}; vertical velocity 1 m s^{-1}; dTrho 1 K. Solid contours positive, dashed contours negative.

4.3.4. Section summary

In summary, convection that occurs at or near the vortex axis produces a monopole of vertical vorticity at low levels and this vorticity persists long after the initial cell decays. Convection is weakest near the vortex axis and the depth of the cyclonic monopole does not extend above a few

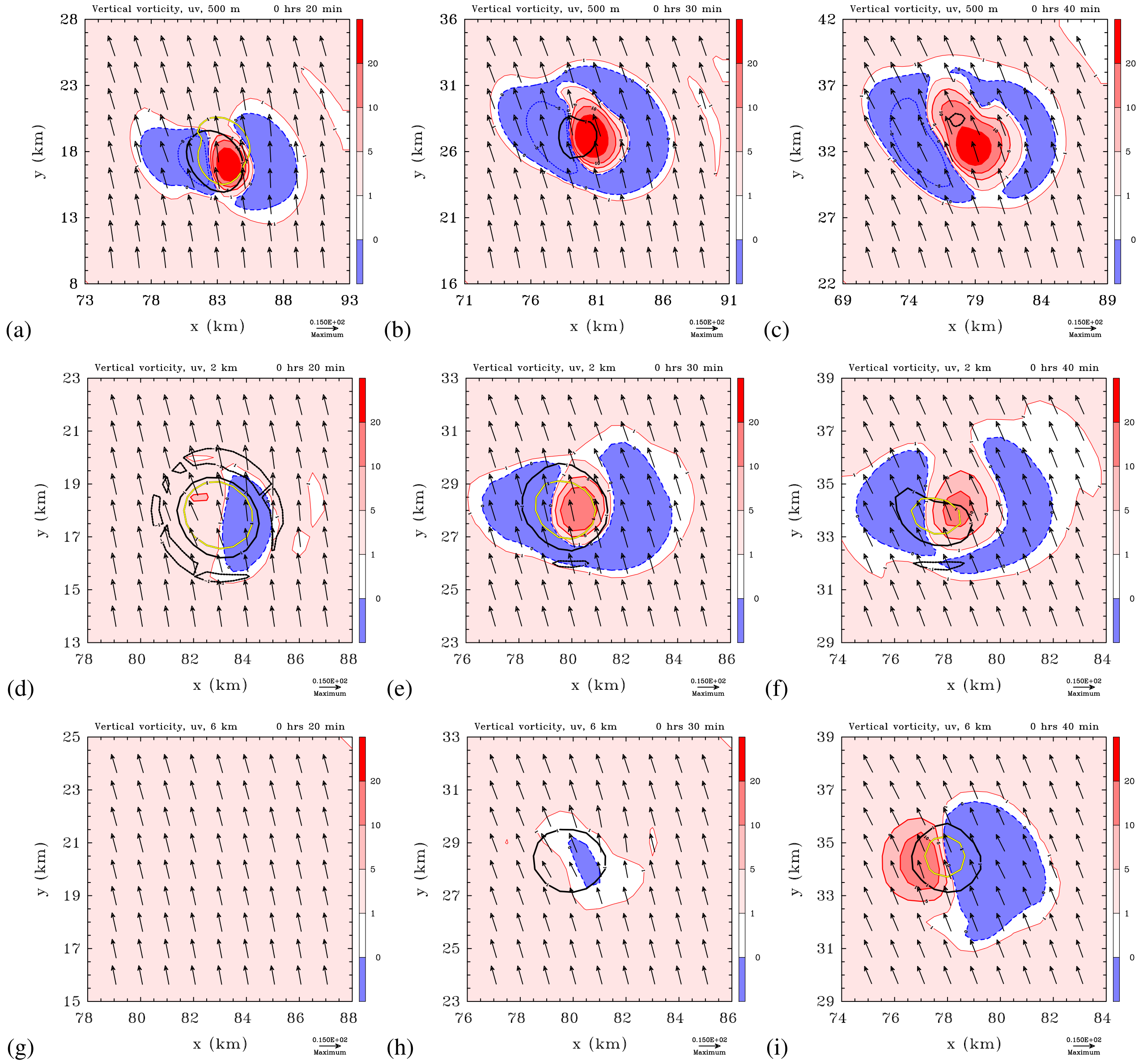

Figure 10. Horizontal cross sections similar to those in Fig. 9 at heights of 500 m (top panels), 2 km (middle panels) and 6 km (bottom panels) at 20, 30 and 40 min for Expt. 4. Contour intervals are the same as in Fig. 9.

kilometres in the vertical. The depth of significant vorticity production is larger, the further the thermal is located from the vortex axis. Anticyclonic vorticity anomalies are weak in convection near the circulation centre.

While convection is generally stronger the further it is located from the vortex axis, the maximum vertical vorticity is weaker and significant anticyclonic anomalies are produced at and beyond the radius of maximum tangential wind. The structure of the vorticity anomalies produced change drastically away from the vortex axis, with monopoles occurring near the axis and dipoles that reverse in sign with height occurring in regions with larger vertical shear near and beyond the radius of maximum winds.

5. Relevance to tropical cyclone genesis and intensification

KS15 suggested that the complexities associated with dipole-like structures of vertical vorticity that reversed in sign with height would have implications for understanding the aggregation of convectively-induced vorticity anomalies during vortex evolution (Nguyen *et al.* 2008, Deng *et al.* 2012). A question that arose was how the anticyclonic anomalies would be ejected from the vortex core so that the aggregation of positive anomalies could occur.

The results of this study suggest that deep convection near the vortex axis doesn't generate appreciable anticyclonic vorticity, and there is no need to invoke complex explanations of how to remove anticyclonic vorticity since so little of it is produced. Near the vortex axis the generation of vorticity is dominated by stretching. Of course, stretching of vorticity will enhance the magnitude of local vorticity anomalies and compression will diminish their magnitude. The stretching and thereby amplification of ambient (or system-scale) vorticity by convection by itself does not lead to an increase in the circulation around a fixed loop embedded in the flow because stretching leads to a contraction in the areal extent of the loop (see Haynes and McIntyre 1987, Raymond *et al.* 2013).

A key result is that significantly enhanced vertical vorticity persists long after the convective cell decays. In developing tropical cyclones, this region of enhanced vorticity can be amplified further should more convection occur nearby. Indeed many recent studies of tropical cyclone genesis found that spin up occurred when repeated bouts of deep convection occurred near the circulation centre (Tory *et al.* 2006a,b, Nolan 2007 Nicholls and Montgomery 2013), Smith *et al.* 2015, Davis 2015, Kilroy *et al.* 2016a, Kilroy *et al.* 2016b).

6. Eddy momentum fluxes

Two additional calculations are carried out to quantify the effect of cloud scale eddies on the evolution of the vortex. The new experiments, Expts. 7 and 8, are similar to Expts. 2 and 4, in which the initial thermal perturbations are located at radii of 25 km and 85 km, respectively. The differences are that surface friction is switched off and a zero gradient lower boundary condition is used. These experiments avoid the clutter from the contribution of the frictionally-induced inflow to the eddy terms that arises in Expts. 2 and 4. However, in terms of cloud evolution, the results are similar to those of Expts. 2 and 4, respectively, the vertical velocity differences being less than about 1 m s^{-1} at all heights (see Table I). In Expts. 7 and 8, ζ_{max} is on the order of 20% larger than in Expts. 2 and 4, respectively, and ζ_{max} is located at the surface instead of at a height of 500 m. The latter differences reflect the increase of vertical vorticity near the surface when frictional processes are switched off.

Following Persing *et al.* (2013), we apply the traditional Eulerian approach of "eddy-mean" partitioning in the azimuthally-averaged tangential velocity equation. Denoting an azimuthal mean of any quantity ψ by the operator $\langle\psi\rangle = \frac{1}{2\pi}\int_0^{2\pi}\psi d\lambda$ and the perturbation therefrom by a prime, ψ', the azimuthal-mean tangential momentum equation has the form:

$$\begin{aligned}\frac{\partial\langle v\rangle}{\partial t} = & -\frac{1}{r^2}\frac{\partial(r^2\langle u\rangle\langle v\rangle)}{\partial r} - \frac{\partial(\langle w\rangle\langle v\rangle)}{\partial z} - f\langle u\rangle \\ & -\frac{1}{r^2}\frac{\partial(r^2\langle u'v'\rangle)}{\partial r} - \frac{1}{\rho}\frac{\partial(\rho\langle v'w'\rangle)}{\partial z} \\ & -c_p\left\langle\frac{\theta'_\rho}{r}\frac{\partial\pi'}{\partial\lambda}\right\rangle + \langle D_v\rangle . \end{aligned} \quad (1)$$

where (u, v, w) is the velocity vector expressed in cylindrical coordinates (r, λ, z), r is the radius, λ is the azimuth, z is the height, ρ is the density (assumed a function of height only), c_p is the specific heat of air at constant pressure, Π is the Exner function $[(p/p*)^\kappa$ where p is the pressure, p^* is a reference pressure normally taken to be 1000 mb and $\kappa = R/c_p$, where R is the specific gas constant], θ_ρ is the density potential temperature (the density temperature in K divided by the Exner function), and D_v is the sub-grid-scale azimuthal component of turbulent stress. In the present formulation, $\langle v\rangle$ is initially equal to the prescribed initial vortex, but is subsequently modified by azimuthal flow perturbation induced by the initial thermal perturbation.

For an isolated convective cloud spanning a small range of azimuths, most of the flow perturbations induced by the initial thermal perturbation will appear in the perturbation velocity (u', v', w'). Our interest here is the magnitude and spatial distribution of $\langle v\rangle$ induced by the deep convective cloud during the first hour of its lifetime and in the contribution thereto from the eddy momentum fluxes: $\langle u'v'\rangle$ and $\langle v'w'\rangle$ (the terms in the second row of Eq. (1)).

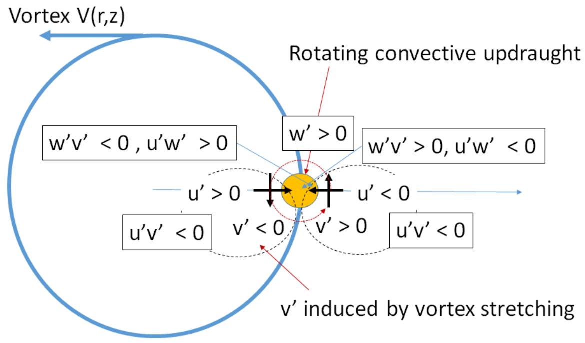

Figure 11. Horizontal cross-section schematic indicating the velocity perturbations induced by a single updraught at some radius from the circulation centre of a cyclonic axisymmetric vortex. The perturbation momentum flux terms about the parent vortex along the centre line of the updraught have signs as shown. See text for discussion.

Some physical insight into the structure of the resolved eddy momentum fluxes can be obtained with schematic as sketched in Fig. 11. Consider the velocity perturbations induced by a single updraught at some radius from the circulation centre of a cyclonic axisymmetric vortex (e.g that shown in Fig. 2). At levels below that where the perturbation vertical mass flux, $\rho w'$ is a maximum, the vertical velocity perturbation w' will be accompanied through continuity by entrainment into the updraught characterized by a radial velocity perturbation u' as shown. The w' perturbation will stretch the existing cyclonic vorticity to produce a positive vertical vorticity perturbation ζ' and an associated tangential wind perturbation v' about the vortical updraught as indicated. At levels above where the perturbation vertical mass flux, $\rho w'$, is a maximum, the perturbations in u' and v' will be reversed.

Panels (a), (b) and (c) of Fig. 12 show radius-height cross sections of the perturbation velocities u', v' and w' at the azimuth of the centre of the thermal perturbation after 20 min in Expt. 7. This time is when the vertical velocity has a maximum at a height of 1 km and is before any downdraught has begun to form. Panels (d) and (e) show the structure of the perturbation momentum flux terms, $u'v'$ and $v'w'$, along the same azimuth. These momentum flux terms have the same signs and structures anticipated from the schematic in Fig. 11. The azimuthal average $\langle v'w'\rangle$ in (panel (g)) has a broadly similar structure to that of $v'w'$ in panel (e), but the structure of $\langle u'v'\rangle$ in panel (f) deviates markedly from that of $\langle u'v'\rangle$ in panel (d). The reason for this deviation is that the structure of $u'v'$ varies considerably with azimuth, unlike that of $v'w'$. This variation is indicated in panels (h) and (i) of Fig. 12, which show the analogous cross sections of $u'v'$, but along azimuths ± 5 deg on either side of that passing through the centre of the thermal perturbation. At the radius of this centre, these cross sections slice the thermal about 2 km from its axis, whereupon there is an appreciable projection of the tangential velocity of the vortical updraught about the axis of the updraught into the radial component along the off-centre cross sections. Likewise, a component of the radial flow perturbation will project on to the tangential component in these cross sections. Together, the asymmetries in perturbation flow account for the differences between the cross sections of $u'v'$ in panels (h) and (i) and that in panel (d). Clearly,

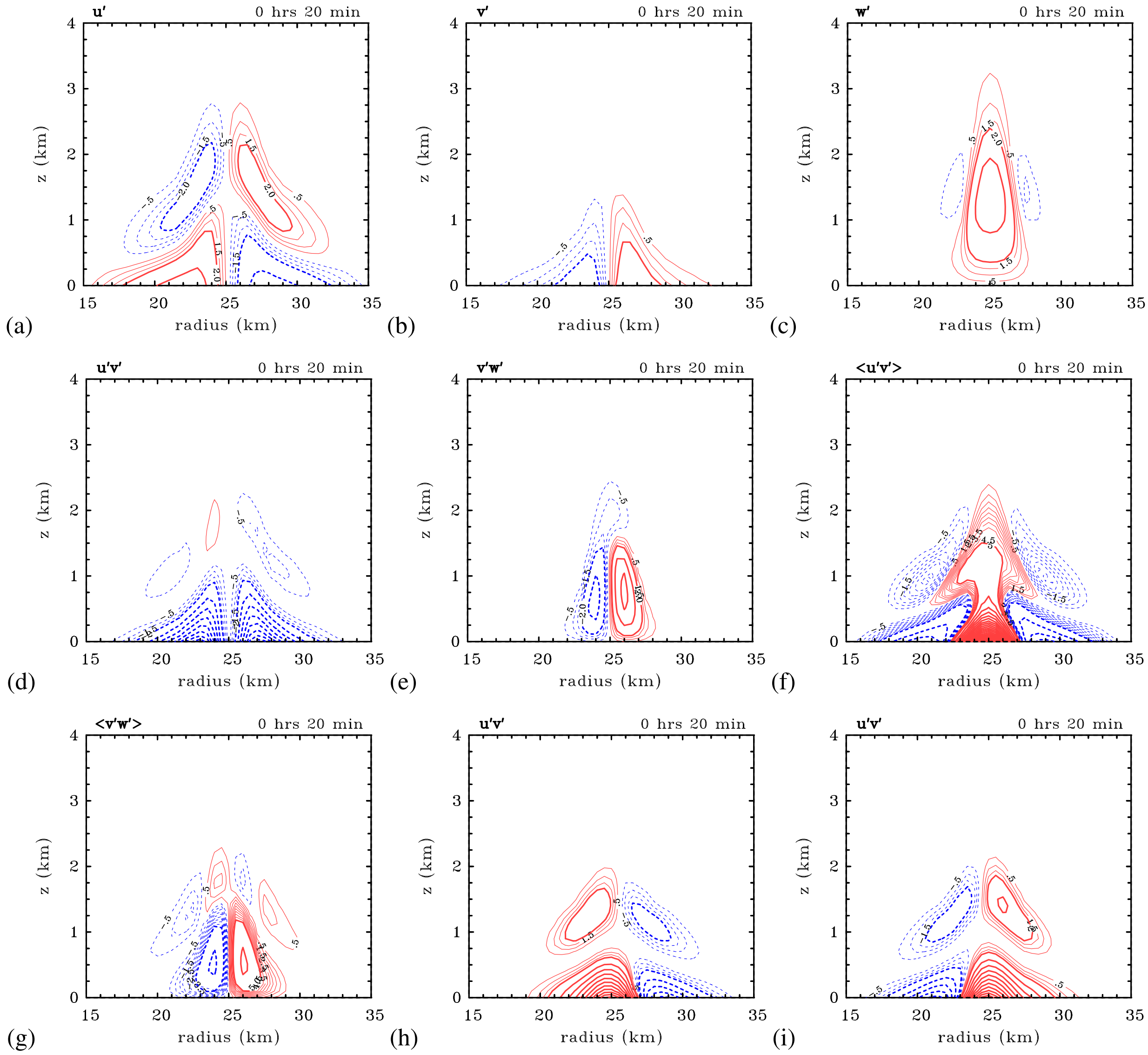

Figure 12. Vertical cross sections at 20 min in Expt. 7 of: (a,b,c) the perturbation velocities u', v' and w' at the azimuth of the centre of the thermal perturbation. Contour interval: thin contours from 0.5 m s^{-1} to 1.5 m s^{-1} in intervals of 0.5 m s^{-1}, thick contours: 2 m s^{-1}. Panels (d) and (e) show the perturbation momentum flux terms, $u'v'$ and $v'w'$, at the azimuth of the centre of the thermal perturbation. Panels (h) and (i) show similar slices of $u'v'$, but along azimuths $+5$ (h) and -5 (i) deg on either side of that passing through the centre of the thermal perturbation. Contour interval: thin contours from 0.5 m^2 s^{-2} to 1.5 m^2 s^{-2} in intervals of 0.5 m^2 s^{-2}, thick contours: 2 m^2 s^{-2}. Panels (f) and (g) show vertical cross sections of the azimuthally averaged flux terms, $\langle u'v' \rangle$ and $\langle v'w' \rangle$. Contour interval: thin contours from 0.5×10^{-2} m^2 s^{-2} to 4.5×10^{-2} m^2 s^{-2} in intervals of 0.5×10^{-2} m^2 s^{-2}, thick contours: 5×10^{-2} m^2 s^{-2}. Solid (red) contours positive, dashed (blue) contours negative.

when calculating $\langle u'v' \rangle$, the positive values of $u'v'$ at 25 km radius in both off centre cross sections compared with small values in the central cross section account for the large positive values of $\langle u'v' \rangle$ in the same region.

While the schematic in Fig. 11 provides useful insight into the structure of the covariance terms, $\langle u'v' \rangle$ and $\langle v'w' \rangle$, we have shown that caution is required not to base the interpretation solely on a single cross section through the centre of the thermal perturbation. Even then, it is derivatives of the covariances that appear in the tendency of $\langle v \rangle$ in Eq. (1). At this point, one has to do the calculation! The upper panels of Fig. 13 show vertical-height cross sections of the individual eddy contributions to $\partial \langle v \rangle / \partial t$ from the terms in the middle row on the right of Eq. (1) and their sum at 20 min for Expt. 7. The principal features of the radial eddy flux contribution $[(1/r^2)\partial \langle -r^2 u'v' \rangle / \partial r]$ is a spin up tendency at low levels (below 1 km, which happens to be approximately the height of $(\rho w)_{max}$) on the outside of the updraught and spin down tendency on the inside (panel (a)). At higher levels the tendency signatures are somewhat weaker. The main features of the vertical eddy flux contribution $[(1/\rho)\partial \langle -\rho r^2 v'w' \rangle / \partial z]$ are similar above a height of 200 m, but opposite in sign below that (panel (b)). Thus when the two contributions are summed, there is some cancellation at low levels and reinforcement aloft (panel (c)). The net result is a positive contribution to the tangential wind tendency radially outside the axis of convection and a negative contribution inside the axis. The maximum tendency of $\langle v \rangle$ at 20 min is 2.1 m s^{-1} h^{-1} in Expt. 7.

Panel (e) of Fig. 13 show the time integrated contribution of the eddy terms to the change in $\langle v \rangle$ over 1 h in Expt. 7. The patterns are similar to the tendencies at 20 min, except for in a shallow layer near the surface and the maximum and

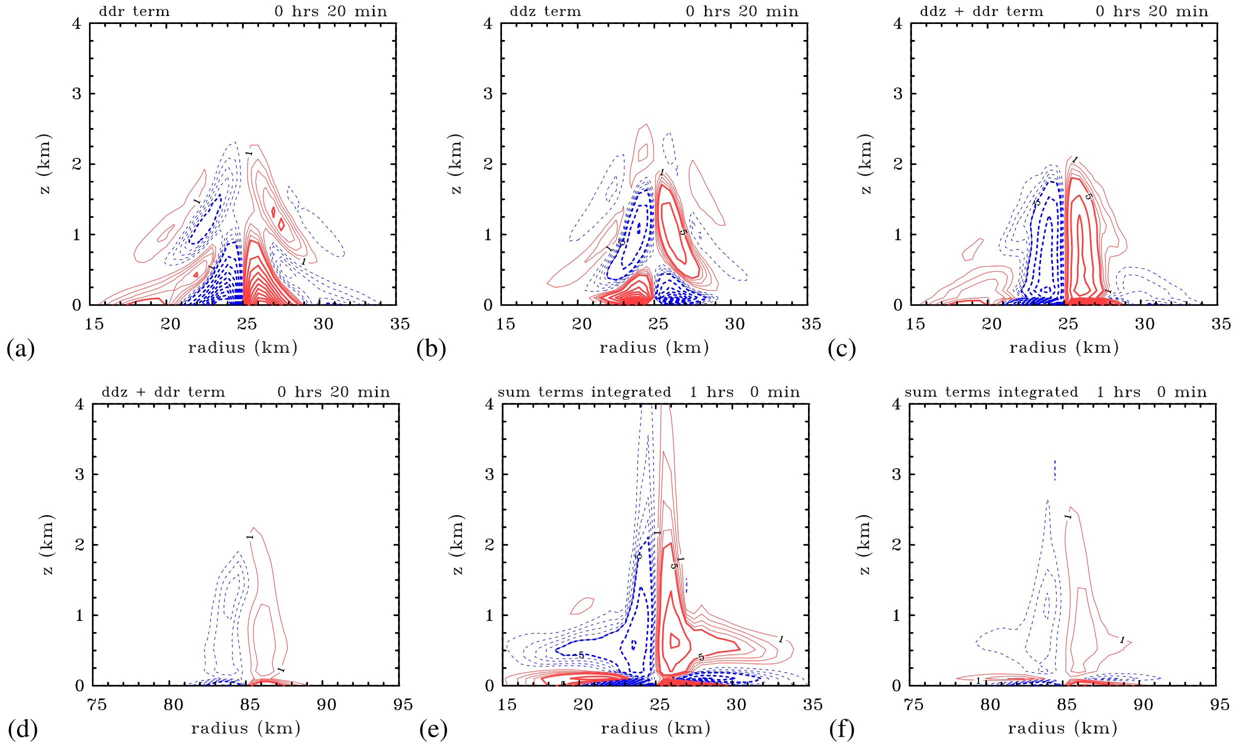

Figure 13. Vertical cross sections at 20 min for Expt. 7 of the (a) radial eddy flux contribution $[(1/r^2)\partial \left\langle -r^2 u'v' \right\rangle /\partial r]$, the (b) vertical eddy flux contribution $[(1/\rho)\partial \left\langle -\rho r^2 v'w' \right\rangle /\partial z]$ and (c) the sum of these terms. Panel (d) shows the sum of these terms for Expt. 8. Contour interval: thin contours 1×10^{-5} m s^{-2} to 5×10^{-5} m s^{-2} in intervals of 1×10^{-5} m s^{-2}, thick contours: 5×10^{-5} m s^{-2}. Panels (e) and (f) show vertical cross sections of the 1 h time-integrated sum of the radial and vertical eddy flux terms in Expts. 7 and 8, respectively. Contour interval: thin contours 1×10^{-2} m s^{-1} to 5×10^{-2} m s^{-1} in intervals of 1×10^{-2} m s^{-1}, thick contours: 5×10^{-2} m s^{-1}. Solid contours positive, dashed contours negative.

minimum values are locally about $\pm$ 0.39 m s^{-1} summed over the hour. The largest difference in the total azimuthally averaged tangential wind field occurs at 34 mins (0.28 m s^{-1}) and this becomes smaller with time (0.15 m s^{-1} at 1 hour). The difference in the tangential wind field is smaller than suggested by the integrated sum of the eddy terms, indicating that diffusion plays a role in weakening the tangential winds over an hour.

When convection is located at a radius of 85 km, the total eddy contribution to $\partial \left\langle v \right\rangle /\partial t$ shown in Fig. 13(d) has a similar pattern to that in Fig. 13(c), but the magnitude is weaker, for the most part because the effect of the updraught is averaged over an annulus with a much larger circumference. The maximum tendency at 20 min is 0.36 m s^{-1} h^{-1} in Expt. 8 (compared to 2.1 m s^{-1} h^{-1} in Expt. 7). The time integrated contribution of the eddy terms to the change in $\langle v \rangle$ over 1 h in Expt. 8 is much weaker than in Expt. 7 (compare panels (e) and (f) of Fig. 13) and these contributions over the hour sum to 0.11 m s^{-1}.

As pointed out by Montgomery and Smith (2016a), in an intensifying tropical cyclone there will be multiple vortical updraughts and these updraughts will excite vortex Rossby and inertia-buoyancy waves, which will in turn contribute also to the sign and structure of the eddy momentum fluxes. We suggest that the foregoing analysis for a single cloud provides a useful starting point for understanding the diagnosed momentum fluxes in this more complex situation.

7. Convective efficiency arguments in vortices

The calculations described herein are pertinent to appraising widely-held ideas concerning the efficiency of deep convection in relation to the radial location of the convection within a typical tropical-cyclone scale vortex. These ideas originated from pioneering analytical calculations by Schubert and Hack (1982) and Hack and Schubert (1986), wherein a fixed spatial distribution of diabatic heating is located at different radii from the vortex centre, where, inter alia, the inertial stability is locally different. Schubert and Hack's argument is that an increase in the local inertial stability acts to impede the strength of the secondary circulation produced by a given heating rate of fixed spatial structure. As a result rising air parcels cool at a lower rate as they expand so that more of the diabatic heating is available to increase their temperature: i.e. the heating is "more efficient" in raising the temperature of the cloud updraught.

The realism of a calculation with fixed heating has been questioned by Smith and Montgomery (2016), who pointed out that, in reality, a reduction of the strength of the secondary circulation in the region of heating would be accompanied by a corresponding reduction in the strength and radial distribution of the diabatic heating rate. The calculations presented here provide an opportunity to quantify the differences in heating rate as a function of radial location, albeit in a situation where the cloud updraught is not assumed to be in approximate hydrostatic balance, unlike the updraught in Schubert and Hack's calculations.

Figure 14 shows time-height series of the maximum diabatic heating rate (characterized here by the material

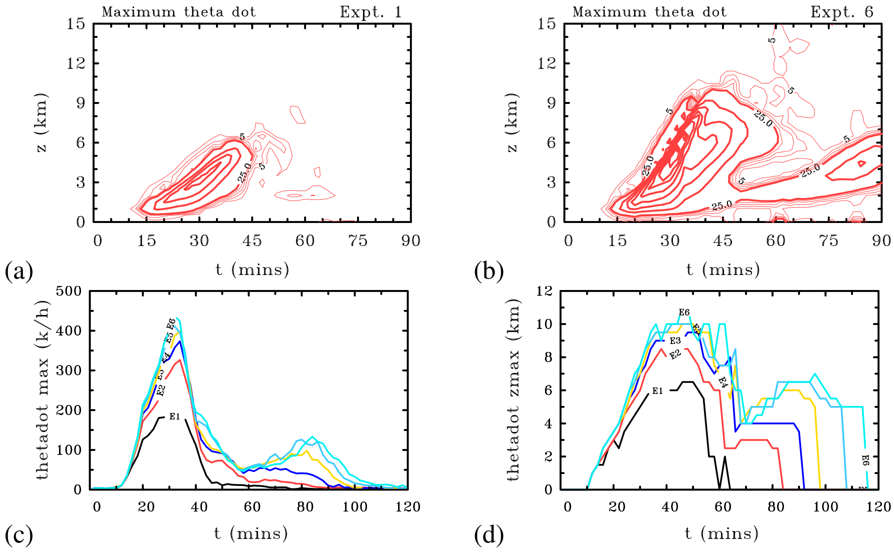

Figure 14. Time-height series of the diabatic heating rate in Expts. 1 and 6 (top panels). Contour interval: 5 K h^{-1} to 20 K h^{-1} in light contours of 5 K h^{-1}, from 25 K h^{-1} in thick contours of 50 K h^{-1}. Panel (c) shows the maximum diabatic heating rate in all experiments as a function of time, and panel (d) shows the maximum height of the 10 K h^{-1} contour.

derivative, $\dot{\theta}$, of potential temperature, θ) at each level and time in the six experiments. Since the pseudo-equivalent potential temperature (θ_e) at the centre of each bubble is essentially the same, the patterns of $\dot{\theta}(t, z)$ are closely related to the corresponding patterns of $w(t, z)$ and it can be seen that there are significant differences in both the depth and magnitude of $\dot{\theta}(t, z)$ in the six experiments. For example, the absolute maximum of $\dot{\theta}$ in Expt 6 (the outermost updraught) is about 20% higher than that in Expt. 1 (the updraught at the vortex centre). Moreover, the vertical extent of diabatic heating in Expt 6 is larger than that in Expt. 1. Notwithstanding that fact that the assumption of the same thermal perturbation has limitations in relation to reality, the results of the thought experiment discussed here adds weight to the arguments presented by Smith and Montgomery (2016). They questioned the realism of assuming a fixed heating rate at different radial locations in the vortex. They noted also the assumption that air parcels rising at different radii have the same θ_e would further limit the realism of calculations that assume a fixed distribution of $\dot{\theta}$ in relation to real tropical cyclones.

8. Conclusions

We have used a series of idealized numerical model simulations to investigate the generation and evolution of vertical vorticity by deep convection in a warm-cored vortex of near tropical storm strength. In these simulations, deep convective updraughts were initiated by thermal perturbations located at different radii from the vortex axis. It was found that, as the location of the thermal perturbation is moved away from the axis of rotation:

(1) the updraught that develops becomes stronger,
(2) the cyclonic vorticity anomaly generated by the updraught becomes weaker,
(3) the structure of the vorticity anomaly changes, and
(4) the depth of the vorticity anomaly increases.

For an updraught along or near the vortex axis, the vorticity anomaly has the structure of a monopole and little or no anticyclonic vorticity is generated in the core. This finding obviates the need in previous simulations of tropical cyclone intensification to explain how anticyclonic vorticity would be expelled from the core of an intensifying vortex when there are multiple clouds contributing to drive the intensification. Vorticity dipoles are generated in updraughts near or beyond the radius of maximum tangential wind speed and this structure reverses in sign with height. In all cases these anomalies persists long after the initial updraught has decayed.

The effects of eddy momentum fluxes associated with a single updraught on the tangential-mean velocity tendency were investigated and a conceptual framework for the interpretation of these eddy fluxes was given. It is found that the eddy fluxes tend to accelerate the azimuthal mean tangential velocity radially outside of the updraught and decelerate it on the inside, consistent with expectations based on the conservation of azimuthal-mean absolute angular momentum. The foregoing effect for a single cloud with a given cross section increases with decreasing radius because the mean circumference of the annulus of averaging decreases relative to the azimuthal extent of the cloud as the radius decreases.

The simulations are used to appraise long standing ideas suggesting that latent heat release in deep convection occurring in the high inertial stability region of a vortex core is "more efficient" than deep convection outside the core in producing temperature rise in the updraught. This conclusion arises from a thought experiment in which the same spatial distribution of diabatic heating is used to force an overturning circulation in regions with different levels of inertial stability. An alternative thought experiment examined here was to force the overturning circulation by initiating convection from the same thermal perturbation. In this case, the diabatic heating associated with the ensuing deep convection decreases with increasing inertial stability and its vertical extent is less. These results add weight to recent arguments questioning the realism of assuming a fixed heating rate at different radial locations in the vortex to demonstrate the efficiency of the heating at higher levels of inertial stability.

9. Acknowledgements

We thank Dr. George Bryan for generously making the model available. Financial support for this research was provided by the German Research Council (Deutsche Forschungsgemeinschaft) under Grant numbers SM30/23-3 and SM30/23-4 and the Office of Naval Research Global under Grant No. N62909-15-1-N021.

References

Bao JW, Gopalakrishnan SG, Michelson SA, Marks FD, Montgomery MT, 2012: Impact of physics representations in the HWRFX on simulated hurricane structure and pressure-wind relationships. *Mon. Wea. Rev.*, **140**, 3278-3299.

Bryan GH, Fritsch JM. 2002: A benchmark simulation for moist nonhydrostatic numerical models. *Mon. Wea. Rev.*, **130**, 2917-2928.

Bryan GH, Rotunno R, 2009: The maximum intensity of Tropical cyclones in axisymmetric numerical model simulations. *Mon. Wea. Rev.*, **137**, 1770-1789.

Črnivec N, Smith RK, Kilroy G, 2016: Dependence of tropical cyclone intensification rate on sea surface temperature. Submitted to *Q. J. R. Meteorol. Soc.*, , (accepted).

Davis C, 2015: The Formation of Moist Vortices and Tropical Cyclones in Idealized Simulations. *J. Atmos. Sci.*, **72**, 3499-3516.

Deng Q, Smith L, Majda A, 2012: Tropical cyclogenesis and vertical shear in a moist Boussinesq model. *Journal of Fluid Mechanics*, **706**, pp 384-412

Fang J, Zhang F, 2010: Initial development and genesis of Hurricane Dolly (2008). *J. Atmos. Sci.*, **67**, 655-672.

Gopalakrishnan SG, Marks FD, Zhang X, Bao JW, Yeh K-S, Atlas R, 2011: The experimental HWRF system: A study on the influence of horizontal resolution on the structure and intensity changes in tropical cyclones using an idealized framework. *Mon. Wea. Rev.*, **139**, 1762-1784.

Hack JJ, Schubert WH, 1986: Nonlinear response of atmospheric vortices to heating by organized cumulus convection. *J. Atmos. Sci.*, **43**, 1559-1573.

Haynes P, McIntyre ME, 1987: On the evolution of vorticity and potential vorticity in the presence of diabatic heating and frictional or other forces. *J. Atmos. Sci.*, **44**, 828-841.

Hendricks, EA, Montgomery MT, and Davis CA, 2004: On the role of "vortical" hot towers in formation of tropical cyclone Diana (1984). *J. Atmos. Sci.*, **61**, 1209-1232.

Kilroy G, Smith RK, 2012: A numerical study of rotating convection during tropical cyclogenesis. *Q. J. R. Meteorol. Soc.*, **139**, 1255-1269.

Kilroy G, Smith RK, Wissmeier U, 2014: Tropical convection: the effects of ambient vertical and horizontal vorticity. *Q. J. R. Meteorol. Soc.*, **140**, 1756-1770.

Kilroy G, Smith RK, 2015: Tropical cyclone convection: the effects of a vortex boundary-layer wind profile on deep convection. *Q. J. R. Meteorol. Soc.*, **141**, 714-726.

Kilroy G, Smith RK, Montgomery MT, 2016a: Why do model tropical cyclones grow progressively in size and decay in intensity after reaching maturity? *J. Atmos. Sci.*, **73**, 487-503.

Kilroy, G, Smith RK, Montgomery MT, Lynch B, Earl-Spurr C, 2016b: A case study of a tropical depression that formed in the Australian Northern Territory (January 2014) in the monsoon trough and intensified over land, as seen in the ECMWF analyses. *Q. J. R. Meteorol. Soc.*, , **in review**.

Montgomery MT, Smith RK, 2014: Paradigms for tropical cyclone intensification. *Aust. Met. Ocean. Soc. Journl.*, **64**, 37-66.

Montgomery MT, Smith RK, 2016: The fluid dynamics of tropical cyclones. *Ann. Rev. fluid Dyn.*, **XX**, in press.

Montgomery MT, Nicholl ME, Cram TA, Saunders A, 2006: A "vortical" hot tower route to tropical cyclogenesis. *J. Atmos. Sci.*, , **63**, 355-386.

Montgomery MT, Davis C, Dunkerton T, Wang Z, Velden C, Torn R, Majumdar S, Zhang F, Smith RK, Bosart L, Bell MM, Haase JS, Heymsfield A, Jensen J, Campos T, Boothe MA, 2012: The Pre-Depression Investigation of Cloud Systems in the Tropics (PREDICT) Experiment: Scientific basis, new analysis tools, and some first results. *Bull. Amer. Meteor. Soc.,* **93**: 153172.

Nguyen SV, Smith RK, Montgomery MT, 2008: Tropical-cyclone intensification and predictability in three dimensions. *Q. J. R. Meteorol. Soc.*, **134**, 563-582.

Nguyen CM, Reeder MJ, Davidson NE, Smith RK, Montgomery MT, 2011: Inner-core vacillations cycles during the intensification of Hurricane Katrina. *Q. J. R. Meteorol. Soc.*, **137**, 829-844.

Nicholls M, Montgomery MT, 2013: An Examination of Two Pathways to Tropical Cyclogenesis Occurring in Idealized Simulations with a Cloud-Resolving Numerical Model. *Atmos. Chem. Phys.*, **13**, 5999-6022.

Nolan DS, 2007: What is the trigger for tropical cyclogenesis? *Aust. Meteorol. Mag.*, **56**, 241-266.

Persing J, Montgomery MT, McWilliams J, Smith RK, 2013: Asymmetric and axisymmetric dynamics of tropical cyclones . *Atmos. Chem. Phys*, **13**, 12249-12341.

Ramsay HA, Doswell CA, 2005: A sensitivity study of hodograph-based methods for estimating supercell motion. *Wea. Forecasting*, **20**, 954-970.

Raymond DJ, Gjorgjievska S, Sessions S, Fuchs , 2013: Tropical cyclogenesis and mid-Level vorticity. *Aust. Met. Ocean. Soc. Journl.*, (submitted).

Rotunno R, Klemp JB, 1982: The influence of the shear-induced pressure gradient on thunderstorm motion. *Mon. Wea. Rev.*, **110**, 136-151.

Rotunno R, Emanuel KA, 1987: An air-sea interaction theory for tropical cyclones. Part II Evolutionary study using a nonhydrostatic axisymmetric numerical model. *J. Atmos. Sci.*, , **44**, 542-561.

Rozoff CM, 2007: Aspects of moat formation in tropical cyclone eyewall replacement cycles. *Ph.D. thesis, Colorado State University*, 165 pp.

Rozoff CM, Schubert WH, McNoldy BD, Kossin JP, 2006: Rapid Filamentation Zones in Intense Tropical Cyclones. *J. Atmos. Sci.*, , **63**, 325-340.

Rozoff CM, Kossin JP, Schubert WH, Mulero PJ, 2009: Internal Control of Hurricane Intensity Variability: The Dual Nature of Potential Vorticity Mixing. *J. Atmos. Sci.*, , **66**, 133147.

Schubert WH, Hack JJ, 1982: Inertial stability and tropical cyclone development. *J. Atmos. Sci.*, , **39**, 1687-1697.

Shin S, Smith RK, 2008: Tropical-cyclone intensification and predictability in a minimal three-dimensional model. **134**, 1661-1671.

Smith RK, 2006: Accurate determination of a balanced axisymmetric vortex. *Tellus*, **58A**, 98-103.

Smith RK, Montgomery MT, 2015: Towards clarity on understanding tropical cyclone intensification. *J. Atmos. Sci.*, , **72**, 3020-3031.

Smith RK, Montgomery MT, 2016: The efficiency of diabatic heating and tropical cyclone intensification . Revised version submitted to Quart. J. Roy. Meteor. Soc. (Jan)

Tory KJ, Montgomery MT, Davidson NE, 2006a: Prediction and diagnosis of tropical cyclone formation in an NWP system. Part I: The critical role of vortex enhancement in deep convection. *J. Atmos. Sci.*, **63**, 3077-3090.

Tory KJ, Montgomery MT, Davidson NE, Kepert JD, 2006b: Prediction and diagnosis of tropical cyclone formation in an NWP system. Part II: A detailed diagnosis of tropical cyclone Chris formation. *J. Atmos. Sci.*, **63**, 3091-3113.

Tory KJ, Davidson NE, Montgomery MT, 2007: Prediction and diagnosis of tropical cyclone formation in an NWP system. Part III: Diagnosis of developing and nondeveloping storms. *J. Atmos. Sci.*, **64**, 3195-3213.

Wissmeier U, Smith RK, 2011: Tropical-cyclone convection: the effects of ambient vertical vorticity. *Q. J. R. Meteorol. Soc.*, **137**, 845-857.